Mechanism of Localized Breakdown of 7000 Series Aluminum Alloys

Shan-Shan Wang,[a,b] G. S. Frankel,[b,*] Jian-Tang Jiang,[a,c] Jun-Feng Chen,[a,b] Sheng-Long Dai,[d] and Liang Zhen[a,z]

[a]*School of Materials Science and Engineering, Harbin Institute of Technology, Harbin 150001, China*
[b]*Fontana Corrosion Center, The Ohio State University, Columbus, Ohio 43210, USA*
[c]*National Key Laboratory of Precision Hot Processing of Metals, Harbin Institute of Technology, Harbin 150001, China*
[d]*Beijing Institute of Aeronautical Materials, Beijing 100095, China*

The localized breakdown behavior of AA7055 alloy, and an Al-Zn-Mg alloy having no Cu, with different tempers was studied in 3.5 wt% NaCl solution by an in situ observation system during polarization. Three potentials at which the current increased rapidly were found for AA7055-T6 (peak-aged) samples. The first breakdown potential corresponded to the transient dissolution of an active surface layer formed during surface preparation by abrading with grinding paper. The second potential at which the current increased rapidly was associated with crevice corrosion and was not a true breakdown potential. The second breakdown potential was associated with pitting of the underlying bulk alloy. However, no surface layer attack and a single breakdown potential were observed for AA7055-T73 (over-aged) samples and for the Cu-free Al-Zn-Mg samples in the peak-aged condition. All three samples contained surface layers consisting of nano-grains with the solute-rich bands formed by surface preparation. Both the Zn-rich bands in the surface layer and the Cu content in matrix solid solution of the underlying bulk alloy are responsible for surface layer attack. The change in pitting potential with over-aged tempers could be rationalized based on the Cu content in the matrix.
© The Author(s) 2013. Published by ECS. This is an open access article distributed under the terms of the Creative Commons Attribution Non-Commercial No Derivatives 4.0 License (CC BY-NC-ND, http://creativecommons.org/licenses/by-nc-nd/4.0/), which permits non-commercial reuse, distribution, and reproduction in any medium, provided the original work is not changed in any way and is properly cited. For permission for commercial reuse, please email: oa@electrochem.org. [DOI: 10.1149/2.080310jes] All rights reserved.

Precipitation-hardenable aluminum alloys are main structural materials for aircrafts due to their high strength-to-density ratio. The Al-Zn-Mg(-Cu) alloys form precipitates following the general precipitation sequence of supersaturated solid solution, GP zones, metastable η', and stable η.[1,2] Metastable η' phase is believed to be the main hardening phase and responsible for the peak hardening in Al-Zn-Mg(-Cu) alloys.[2] The equilibrium phase η has the hexagonal structure of $MgZn_2$, but Al and Cu can substitute for Zn, and the stoichiometry of this phase can be described as $Mg(Zn,Al,Cu)_2$ in Cu containing $7\times\times\times$ series Al alloys.[3,4] Aging treatments produce changes in the morphology, chemistry, size and density of precipitates and the composition of the solid solution. In the past decade, much research effort has been put into evaluating the composition of nanoscale precipitates in Al alloys due to the development of advanced characterization tools such as atom probe tomography (APT).[2,5–7] Sha and Cerezo studied the chemistry evolution of the early-stage precipitates in 7050 Al alloy using transmission electron microscopy (TEM) and APT.[2] Marlaud and Deschamps investigated the composition of precipitates and the solid solution in Al-Zn-Mg-Cu alloys in peak-aged and over-aged conditions by combining APT and systematic anomalous small-angle X-ray scattering (ASAXS) techniques.[7] This microstructural information has also facilitated a better understanding of corrosion behavior in $7\times\times\times$ series Al alloys with different heat treatments.

The localized breakdown behavior of $7\times\times\times$ series Al alloys has been studied extensively.[4,8–12] The anodic polarization curve for $7\times\times\times$-T6 Al alloys in NaCl solution exhibits two breakdown potentials. However, only one breakdown potential is observed for $7\times\times\times$-T73 Al alloys. Maitra and English attributed the first breakdown of 7075-T6 Al alloy to the pitting of the solute-enriched grain boundary region and the second one to the pitting of the matrix.[8] The single breakdown potential for 7075-T73 Al alloy was considered to be related to the pitting of the Cu depleted solid solution matrix. Meng and Frankel studied the corrosion behavior of AA$7\times\times\times$-T6 alloys with various Cu contents.[9] Two breakdown potentials were observed for Cu-containing AA$7\times\times\times$-T6 alloys in deaerated NaCl solution, the values of which increased logarithmically with increasing Cu content.

The first breakdown potential was observed to be associated with the transient dissolution of a thin surface layer, which was considered to be due to the uniform attack of the Al matrix including the fine hardening precipitates. However, a single breakdown potential and no surface layer attack were found for the Cu-free T6 peak-aged alloy. Huang and Isaacs observed that the streaking corrosion occurred on as-abraded AA7075-T6 alloy, which was due to a susceptible surface layer.[10] Zhao and Frankel studied the mechanism of the first breakdown in AA7075 alloy using an in situ observation system.[11] They also prepared the cross-sectional TEM samples using focused ion beam (FIB), which preserved the surface layer formed by polishing, and characterized the surface microstructure using scanning TEM (STEM). The first breakdown potential of the as-polished AA7055-T6 alloy was associated with the dissolution of an active surface layer, which contained nano-grains with the solute-rich bands formed by polishing. The Zn-rich bands were thought to be responsible for layer attack. However, the Zn-rich bands were also observed for the over-aged alloy, which did not exhibit layer attack.[12] The cause of surface layer attack is still controversial. Kappes and Frankel investigated the corrosion behavior of 7050 Al alloy with different tempers with the information of the microstructure evolution provided by APT and TEM.[13] They suggested that the surface layer attack occurred on the 7050 Al alloy with microstructures in which η' precipitates were the dominant hardening phase.

Deformed surface layers with microstructure containing ultrafine grains can form on various metals and alloys subjected to severe plastic deformation such as equal-channel angular pressing,[14] high pressure torsion,[15] machining[16] and rolling.[17] Ultrafine-grained microstructures in the surface layer of 7075 Al alloy were generated by ultrasonic shot peening.[18] Forsyth reported that superficial corrosion attack occurred on machined surfaces of 7010 Al alloy in seawater. He suggested that the attack of an outer layer of the machining-induced deformation zone was responsible for superficial corrosion.[16] The studies of Afseth and his co-workers[17] showed that a highly deformed near-surface region on AA3005 was produced by shear deformation during rolling. This deformed layer was preferentially attack during corrosion process after high temperature heat-treatment, which was due to secondary precipitation promoted by high deformation and correspondingly depletion of noble alloying elements in solid solution in this region.

*Electrochemical Society Fellow.
[z]E-mail: lzhen@hit.edu.cn

The goal of this work was to characterize the polarization behavior of 7××× series Al alloys with different microstructures, in order to determine the factors that control the surface layer attack and matrix breakdown. A commercial AA7055 alloy in peak-aged and over-aged conditions and a Cu-free Al-Zn-Mg alloy in the peak-aged condition were used in this work. An in situ optical technique was used to record the surface changes during electrochemical polarization. The surface microstructure was characterized using STEM, which provided a better understanding of the relationship between the microstructure and localized breakdown behavior of 7××× series Al alloys.

Experimental

AA7055 alloy with chemical compositions of Al-7.76Zn-1.94Mg-2.35Cu (wt%) was used in the current investigation. Samples of 15 mm × 15 mm × 5 mm were solution heat treated at 480°C for 1 h, quenched in water to room temperature, and then artificially aged to T6 peak-aged and T73 over-aged conditions. Samples were aged at 120°C for 24 h to create the T6 peak-aged temper. The T73 over-aged temper consisted of two-step aging treatment, first at 120°C for 6 h followed by aging for 24 h at 163°C. To determine the effects of Cu content on polarization behavior of 7××× series Al alloys, Al-4.59Zn-1.48Mg-0.0058Cu (wt%) was used as comparison in this work. This alloy contains only 0.0058 wt% Cu and can be considered to be Cu-free. A common heat-treatment to achieve the T6 peak-aged temper as mentioned above was carried out on the Cu-free alloy. All the samples were mechanically ground in ethyl alcohol with SiC paper of different grits for different final surface roughness as discussed below. Grinding was performed in ethyl alcohol to minimize corrosion.

Vickers hardness measurements on Al alloys were performed. A 200 g load and a hold time of 20 s were used. Electrochemical potentiodynamic polarization measurements were performed using a Gamry PC4/FAS1 potentiostat. A saturated calomel electrode (SCE) and Pt counter electrode were used. The potentiodynamic polarization curves of samples with different aging treatments were measured in aerated and deaerated 3.5 wt% NaCl solution. The solution was deaerated with Ar gas to decrease the corrosion potential and separate it from the breakdown potential. Samples were held at the open-circuit potential (OCP) for 0.5 h and then anodically polarized from the OCP. Two scan rates of 0.167 and 0.03 mV/s were used. The slower scan rate allowed for clear observation of the characteristics of the polarization curves. Some of the samples were masked by red lacquer to exposure small area and placed in a special vertical cell under an optical microscope for in situ observation of the corroded surface during polarization tests. The details about this technique have been reported previously.[11]

The microstructures of 7××× series Al alloys were characterized using optical microscopy (OM) and STEM. OM was used to observe the surface morphology after polarization tests. TEM foils for characterizing the precipitates in the bulk alloy were prepared by twin-jet polishing at 30 V using a solution of 30% nitric acid and 70% methanol cooled to −30°C. The cross-sectional TEM samples for characterizing the surface microstructure were prepared by FIB using a 30 keV Ga ion beam and 5 keV electron beam. The cross-sectional TEM samples were 15 μm long, 5 μm deep into the bulk and 100 nm thick. These samples were cut along the final abrasion direction as indicated by the scratches on the surface. Before FIB cutting, platinum was deposited on the surface of samples in the FIB to avoid surface damage. TEM (STEM) characterization of precipitates and composition was conducted with a JEOL 2100 operated at 200 kV and an FEI Tecnai F30 operated at 300 kV. Drift-corrected energy-dispersive spectroscopy (EDS) line profiles were performed in STEM mode. The probe size was less than 3 nm and the step size of the beam scan was 1 nm.

Results

Polarization behavior of the AA7055-T6 alloy.— Figure 1 shows the anodic potentiodynamic polarization curve for the AA7055-T6 sample abraded to 320 grit in aerated 3.5 wt% NaCl solution polarized at a scan rate of 0.03 mV/s. Three potentials at which the current
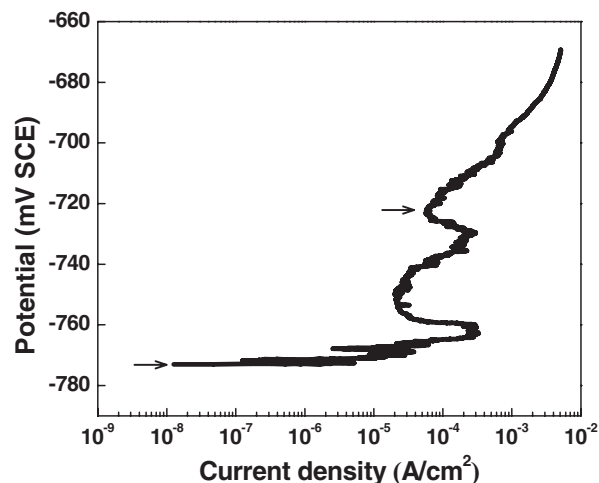
Figure 1. Anodic polarization curve for the as-abraded (320 grit) AA7055-T6 sample in aerated 3.5 wt% NaCl solution at a scan rate of 0.03 mV/s. The arrows point out the two breakdown potentials. Note that the increase in current at −740 mV SCE is associated with crevice corrosion. This potential is not a true breakdown potential.

increased rapidly were observed for this as-abraded sample. Previous studies have shown that anodic potentiodynamic polarization curves for Cu-containing AA7×××-T6 samples in both aerated and deaerated NaCl solution exhibit two breakdown potentials.[9,11]

The video from this experiment[19] shows the animated polarization curve and synchronized video images for the as-abraded (320 grit) AA7055-T6 alloy in aerated 3.5 wt% NaCl solution. Several black spots appeared on the as-abraded shiny surface during the OCP condition. It is likely that these spots were associated with the attack of intermetallic particles (IMPs) or the matrix phase surrounding IMPs. The dark spots were seen to grow and detach from the surface during anodic polarization, and so it is assumed that they were hydrogen gas bubbles that were associated with active dissolution of Al in the pits that formed even during OCP exposure.[20] The fact that the pits formed at the OCP and the current increased rapidly as the potential was scanned in the positive direction from the OCP indicates that the OCP (∼ −775 mV SCE) was pinned close to the first breakdown potential. The surface images show the gray patches that initiated at the first breakdown potential and then spread out across the surface as a layer. The expanding patches moved very fast along the final abrasion direction as indicated by the scratches on the surface. The current reached a peak and then decreased because the total amount of patch perimeter decreased as the surface layer was consumed.[11] The images show that the gray patches continued to spread until the whole surface layer almost dissolved. Then obvious corrosion activity on the exposed surface seemed to cease, indicating that the surface repassivated. The first breakdown potential in as-abraded AA7055-T6 alloy is related to the transient dissolution of an active surface layer formed by surface preparation, in agreement with previous results for 7××× series Al alloys.[11,13]

The current started to increase again as the applied potential was increased just above about −740 mV SCE. This current increase in the potential region from about −740 mV SCE to −730 mV SCE was primarily associated with crevice corrosion as evidenced by hydrogen gas bubbles along the edge of the red lacquer mask. It has been suggested previously that the samples exhibiting surface layer dissolution were very susceptible to crevice corrosion under the edge of the mask, because the active surface layer extended on the surface beneath the lacquer mask.[11,13] There were some evidences of metastable pitting in this potential range, as indicated by small hydrogen bubbles at specific spots on the surface. However, most of the hydrogen bubbles accumulated at the edge of the mask from crevice activity. As the applied potential was further stepped upward, the current decreased again to a second minimum. The surface repassivated again as crevice
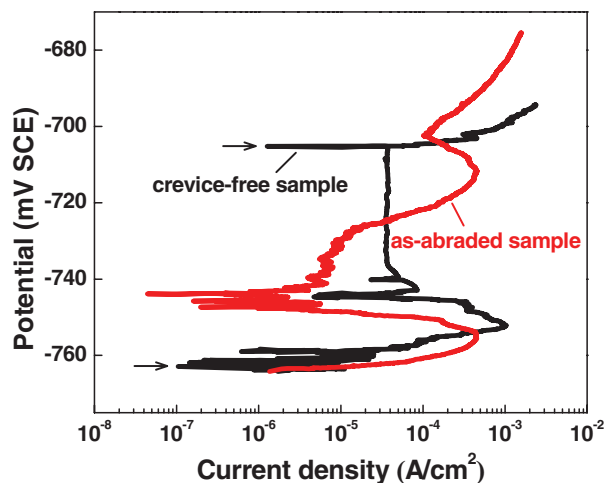
Figure 2. Anodic polarization curves for crevice-free and as-abraded (1200 grit) AA7055-T6 samples in aerated 3.5 wt% NaCl solution at a scan rate of 0.03 mV/s. The arrows point out the two breakdown potentials.

Figure 3. Anodic polarization curves for etched and as-abraded (320 grit) AA7055-T6 samples in aerated and deaerated 3.5 wt% NaCl solution at a scan rate of 0.167 mV/s. The arrows point out the breakdown potentials.

corrosion and metastable pitting seemed to cease. The second increase in current therefore does not reflect the presence of a true breakdown potential, but only the stability of crevice corrosion under the mask edge as was found previously for AA7075 alloy.[11] Stable localized corrosion occurred across the exposed surface area at potentials above the second breakdown potential, about −720 mV SCE.

To further identify the cause of the second current peak, crevice-free samples were prepared. The details about crevice-free samples preparation have been reported previously.[11] Briefly, it involves removing the active layer on the whole surface by dissolution, except for a small spot. The masking layer is then applied to the matrix metal, not on the active surface layer.

The anodic polarization curves for crevice-free and as-abraded (1200 grit) AA7055-T6 samples in aerated solution are shown in Figure 2. Both samples exhibited layer attack as the current increased sharply above the OCP, which was pinned at the first breakdown potential. The current then decreased on both samples as the exposed active surface layer was consumed. The differences in the polarization curves for the as-abraded samples in Figures 1 and 2 result from the effects of the final grinding paper (320 grit vs. 1200 grit), but the form is similar. The 1200 grit abraded sample also exhibited a second increase in current starting at about −730 mV SCE as the result of crevice corrosion under the mask edge. The current then increased above the second breakdown potential at around −700 mV SCE from pitting across the surface.

The crevice-free sample abraded to 1200 grit exhibited a current peak after the first breakdown potential associated with layer attack (Figure 2). After this peak, the current decreased, and then became cathodic and constant over a range of about 40 mV. The rate of anodic reactions in this region was lower than the rate of the cathodic reaction (oxygen reduction) for a sample without crevice corrosion. The current then switched to anodic again and increased rapidly at potentials above about −705 mV SCE, the second breakdown potential associated with pitting across the surface.

The surface layer formed during polishing can be removed by means of ion milling or chemical etching.[11] Etching was performed on samples abraded to 320 grit in 1.0 M NaOH at 60°C for 1.5 min followed by immersion in 70% HNO₃ for 0.5 min. The current density increased rapidly as the potential was increased above OCP for the chemically etched samples polarized in either aerated or deaerated NaCl solution at a scan rate of 0.167 mV/s (Figure 3). The OCP was pinned close to the single breakdown potential at about −700 mV SCE. This potential is close to the second breakdown potential for unetched samples, and was also the result of pitting corrosion across the surface. Neither thin-film dissolution nor crevice corrosion was observed, as shown in the video of the etched sample.[21]
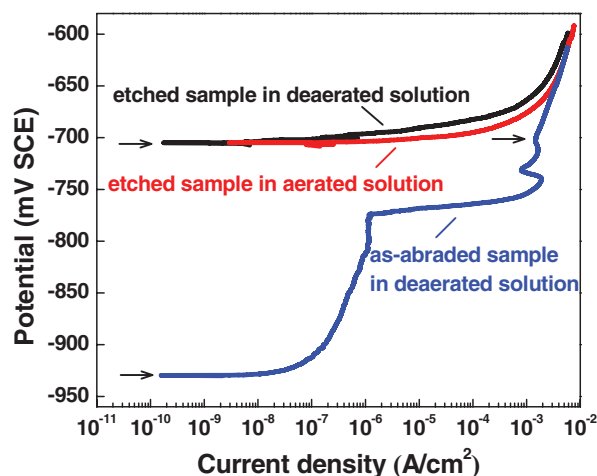
The polarization curve for the as-abraded (320 grit) sample in deaerated solution shows a stable passive region for a range of potentials above the much lower OCP (Figure 3). In the absence of oxygen, the OCP was not pinned at the first breakdown potential, which can clearly be identified with a sharp increase in current at about −770 mV SCE. This value is close to the OCP in aerated tests, which was pinned at the first breakdown potential, and layer attack was also observed starting at this potential in deaerated solution. A peak associated with crevice corrosion followed by an increase in current from pitting corrosion was also observed for this as-abraded peak-aged sample in deaerated solution.

The fact that the OCP for the etched sample in deaerated solution was not lowered and the passive region was not revealed, while these characteristics were observed for the as-abraded sample, suggests that the passive current density was reduced after etching to a value smaller than the rate of cathodic reaction so that the intersection of the partial anodic and cathodic curves was at the first breakdown potential. To further determine the effects of chemical etching in alkaline solution on the surface of the AA7055-T6 samples, the cathodic polarization curves for etched and as-abraded peak-aged samples (320 grit) in deaerated solution were measured (Figure 4). The etched sample exhibited a much higher OCP and a region where the cathodic current density was about 0.2 μA/cm², independent of potential. This
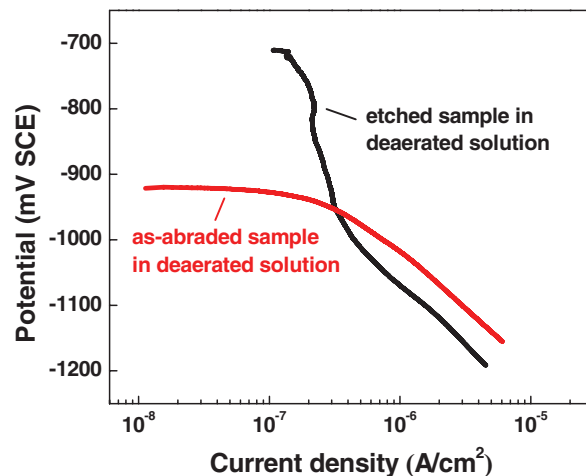
Figure 4. Cathodic polarization curves for etched and as-abraded (320 grit) AA7055-T6 samples in deaerated 3.5 wt% NaCl solution at a scan rate of 0.167 mV/s.
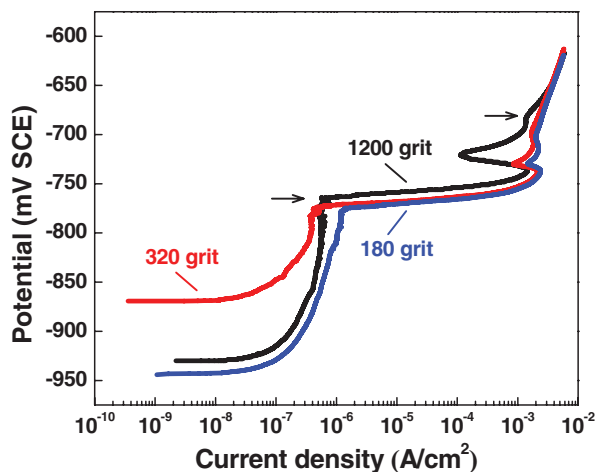
Figure 5. Anodic polarization curves for as-abraded AA7055-T6 samples with different surface roughness in deaerated 3.5 wt% NaCl solution at a scan rate of 0.167 mV/s. The arrows point out the two breakdown potentials.

lack of potential dependence suggests that the reaction was associated with oxygen reduction. Oxygen reduction is generally not observed in deaerated solution, but the very low value of limiting current density indicates that this current was associated with the reduction of a small amount of residual oxygen remaining in the cell despite the deaeration by bubbling of Ar. This region of oxygen reduction was not observed for the as-abraded sample. These differences can be explained by differences in passive current density. The passive current density for the etched sample must be less than $0.2\ \mu A/cm^2$ because the rate of residual oxygen reduction was at this value. In contrast, the passive current density for the as-abraded sample (320 grit) is seen to be about $1\ \mu A/cm^2$ in Figure 3. Changes in the surface associated with etching seem to result in a significant decrease in passive current density.

Because an active surface layer forms during surface preparation in 7×××× series Al alloys,[11–13] it is likely that the electrochemical properties are influenced by the surface roughness through changes in the surface layer. The anodic polarization curves for AA7055-T6 samples abraded to 180, 320 and 1200 grit in deaerated solution are shown in Figure 5. The roughness did not change the shape of the polarization curves, but there were small differences in the values of the breakdown potentials.

Polarization behavior of the AA7055-T73 alloy.— Figure 6 shows the anodic polarization curves for the AA7055-T73 samples abraded
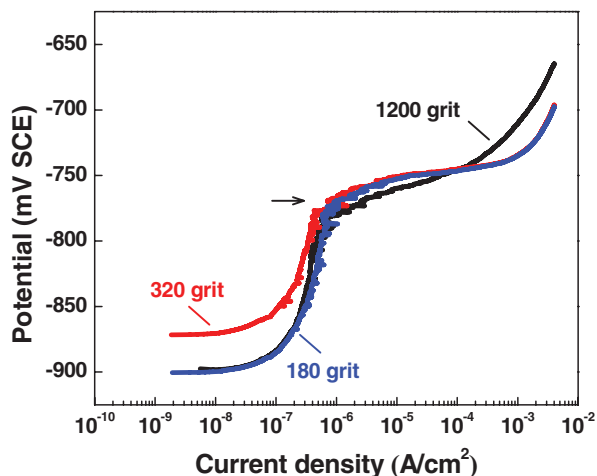
Figure 6. Anodic polarization curves for as-abraded AA7055-T73 samples with different roughness in deaerated 3.5 wt% NaCl solution at a scan rate of 0.167 mV/s. The arrow points out the single breakdown potential.
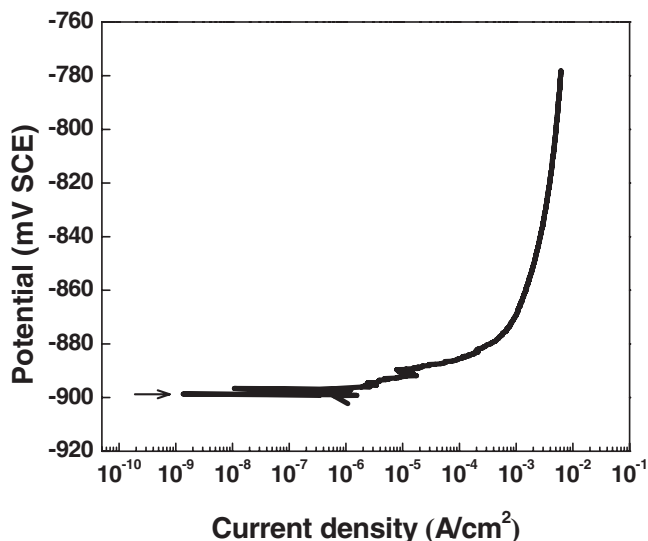
Figure 7. Anodic polarization curve for the Cu-free Al-Zn-Mg sample in the T6 peak-aged temper in aerated 3.5 wt% NaCl solution at a scan rate of 0.167 mV/s. The arrow points out the single breakdown potential.

to 180, 320 and 1200 grit in deaerated solution. Only one breakdown potential was found for T73 over-aged samples with different surface roughness. The over-aged samples behaved identically even polarized at a scan rate of 0.03 mV/s (not shown here). Neither surface layer attack nor crevice corrosion was observed, as shown in the video of this sample abraded to 1200 grit.[22] Stable localized corrosion occurred above the single breakdown potential (about −770 mV SCE). Interestingly, the pitting potential of the T73 over-aged samples, about −770 mV SCE, was markedly lower than that of the T6 peak-aged samples (the second breakdown potential), which was about −700 mV SCE (320 grit in Figure 5).

Polarization behavior of the Cu-free Al-Zn-Mg alloy in the T6 peak-aged temper.— The anodic polarization curve for the Cu-free Al-Zn-Mg sample in the T6 peak-aged temper abraded to 1200 grit in aerated solution is shown in Figure 7. In contrast to the as-abraded AA7055-T6 sample, the Cu-free sample exhibited only one breakdown potential, and many pits were observed by the unaided eye with no evidence of surface layer attack. In aerated solution the OCP of the Cu-free alloy, about −900 mV SCE, was pinned close to the pitting potential, and was much lower than both breakdown potentials of the as-abraded AA7055-T6 samples. These results are in close agreement with previous work.[9] The corrosion morphology in the earlier work indicated that surface layer dissolution was found for all except for the Cu-free Al alloy, although this study was performed before the notion of surface layer dissolution was proposed and developed. This indicates that the Cu content in the Al alloy plays a critical role in both layer attack and localized corrosion of the underlying bulk alloy.

Corrosion morphology of as-polarized samples.— Samples were characterized by OM after potentiodynamic polarization to high potentials. The AA7055-T6 sample abraded to 1200 grit (Figure 8a) exhibited dark corrosion product uniformly covering the originally shiny surface. The video of the as-abraded (320 grit) AA7055-T6 sample[19] suggests that the corrosion product layer was produced by surface layer attack. Large pits (indicated by arrows) can be seen under the edge of the ring, along the boundary between corroded and uncorroded zone. These large pits apparently formed underneath the thin-film product, which generated several hydrogen gas bubbles at the edge of the mask as indicated in the video of this sample.[19] However, many pits and no homogeneously dark corrosion product were found on the shiny surface in the AA7055-T73 sample exhibiting no
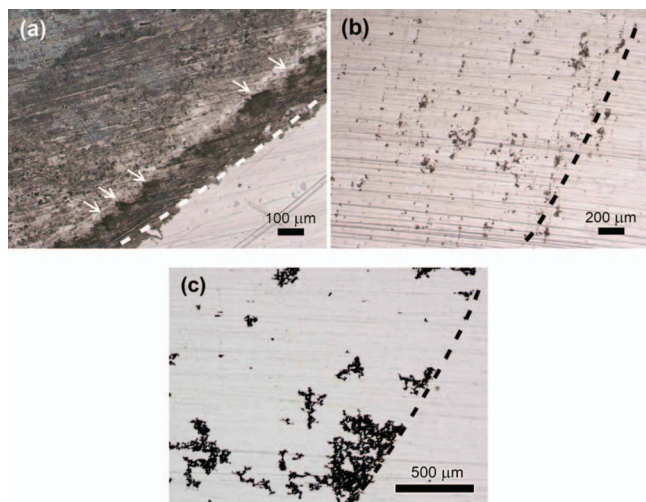
Figure 8. Optical micrographs of as-abraded (1200 grit) (a) AA7055-T6, (b) AA7055-T73, and (c) Cu-free alloy T6 peak-aged samples after potentiodynamic polarization to high potentials. The arrows in (a) point out large pits. The boundary between the surface exposed and unexposed to the NaCl solution during polarization has been schematically drawn in dashed lines.

surface layer dissolution (Figure 8b). The Cu-free sample in the peak-aged temper (Figure 8c) also exhibited only pits on the smooth surface after polarization. Uniform corrosion product after polarization tests can be seen as an evidence of surface layer dissolution.

Microstructure of the bulk substrate of AA7055-T6 and T73 alloys.— Figure 9 shows bright-field TEM images taken from close to the ⟨011⟩ zone axis of the Al matrix in AA7055-T6 and T73 alloys. Both samples contain a very high density of precipitates. The T6 peak-aged sample contains mostly metastable η′ precipitates, in close agreement with previous results.[2,6,23] Two of four possible η′ variants are visible edge-on, and the two others are observed as ellipsoid shape (Figure 9a). However, some η precipitates have already formed, and GP zone diffraction spots are also observed in the Al ⟨001⟩ SADP for the AA7055-T6 sample.[23] Metastable η′ phase is considered to be the main hardening phase in peak-aged Al-Zn-Mg-Cu alloys.[2,23] Metastable η′ phase with platelet morphology has a hexagonal structure, with a habit plane $(0001)_{η′}$ that is parallel to the $(111)_{Al}$ planes, and is coherent with the Al matrix.[6,23] Compared to the T6 peak-aged sample, the T73 over-aged sample has a larger precipitate size (Figure 9b). Both η′ and η precipitates coexist in the matrix microstructures of the T73 over-aged sample, and the latter are dominant. The equilibrium η phase also has a hexagonal structure and the same morphology as η′ phase, but is incoherent with the Al matrix.[23] The formation of η phase often leads to the decrease in strength of 7××× series Al alloys. Accordingly, the Vickers hardness of the T73
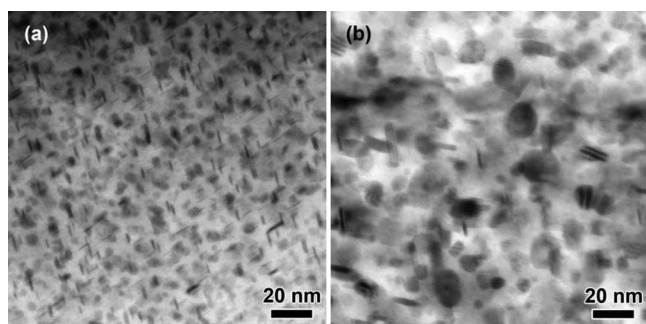
Figure 9. TEM bright-field images of the bulk substrate showing the precipitates microstructures in (a) the T6 peak-aged sample and (b) the T73 over-aged sample.
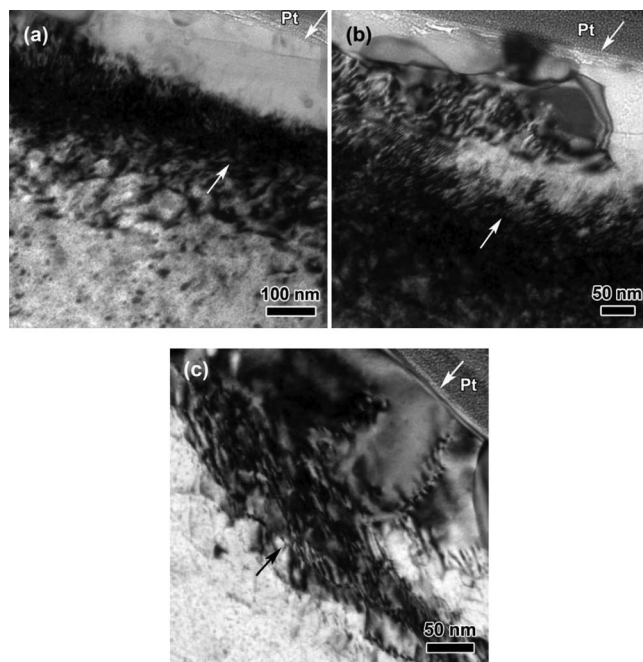
Figure 10. TEM bright-field images in the cross-sectional AA7055-T6 sample showing (a) the surface layer containing fewer and smaller precipitates, (b) nano-grains in the surface layer, and (c) dislocation walls that become subgrain boundaries. The arrows point out the surface layer.

over-aged alloy, 157.8, is lower than that of the T6 peak-aged alloy, 178.9.

Microstructure of the extreme surface region of as-abraded samples.— Figure 10 shows bright-field TEM images of the cross-sectional AA7055-T6 sample. Tilting the foil in TEM reveals different contrasts from defects such as dislocations. A unique surface layer about 300 nm on average in thickness (measured from TEM and HAADF images) is located between the protective Pt layer and the bulk substrate material. There are fewer and smaller precipitates in the surface layer than those in the bulk matrix (Figure 10a). A very high density of dislocations is visible along the interface between the surface layer and the bulk matrix. Sub-boundaries and dislocations were observed when the foil was tilted in TEM. The surface layer can be seen to consist of nano-grains (Figure 10b). Some of nano-grains are subgrains as evidence by dislocation walls that become subgrain boundaries (Figure 10c).

The cross-sectional microstructures of this as-abraded sample were also characterized by high-angle annular detector dark-field scanning transmission electron microscope (HAADF-STEM). In HAADF-STEM mode, the intensity depends on atomic number (Z) only and thus the bright contrast indicates high atomic number elements such as Cu or Zn.[24] The HAADF image (Figure 11) shows that the surface layer of the as-abraded (1200 grit) sample contained some large second phase particles enriched in high Z number elements. However, there are fewer and smaller precipitates inside the surface layer than those in the bulk matrix, in agreement with the TEM results. Bright brands are evident, which means heavy atomic elements are enriched at the nano-grain boundaries. The cross-sectional STEM samples cut perpendicular to the final polishing direction were characterized in the earlier work.[11] They suggested that surface layer contained high aspect ratio nano-grains elongated along the final polishing direction. An EDS line scan with a step size of 1 nm was measured across a bright band (Figure 12). The bright band was enriched in Cu, Mg and Zn, as was found previously for the abraded AA7075-T6 alloy.[11] It is of interest that the level of Zn K to Al K was lower than that of Cu K to Al K and Mg K to Al K inside the surface layer (Figure 12b).
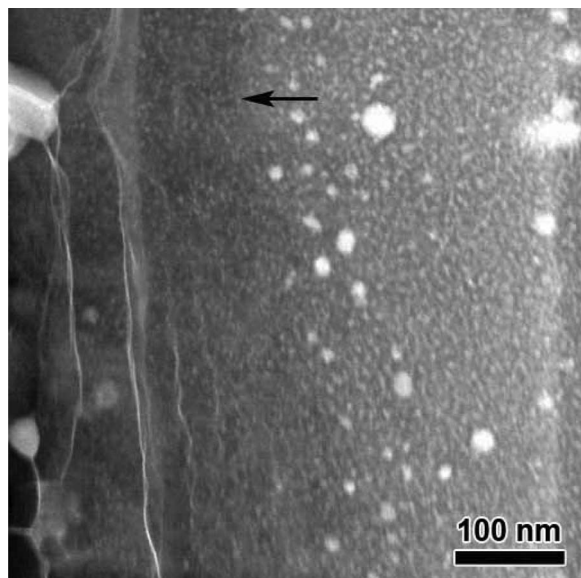
Figure 11. HAADF image of the cross-sectional AA7055-T6 sample. The arrow points out the surface layer.
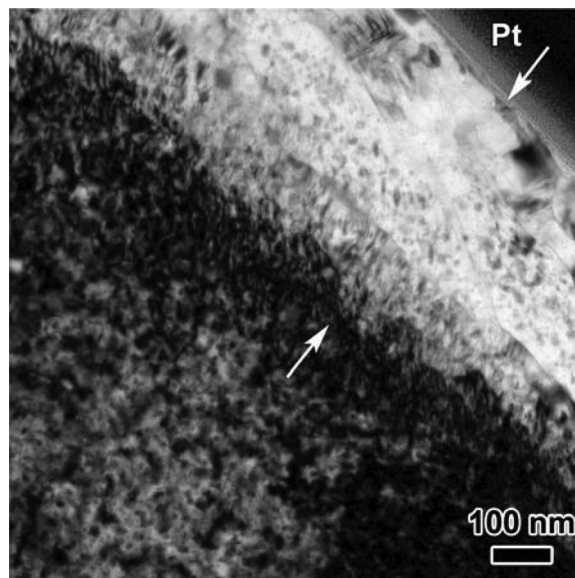
Figure 13. TEM image of the cross-sectional AA7055-T73 sample abraded to 1200 grit. The arrows point out the surface layer.

However, Zn K/Al K reached the same level as Cu K/Al K and Mg K/Al K in the bulk matrix. To discern more clearly the compositional change across the bright band, the scan was expanded close to the bright band (Figure 12c).

TEM and HAADF images of the cross-sectional AA7055-T73 sample abraded to 1200 grit are shown in Figures 13 and 14a, respectively. The T73 over-aged sample also exhibits a unique surface layer consisting of nano-grains with bright bands, although it was shown
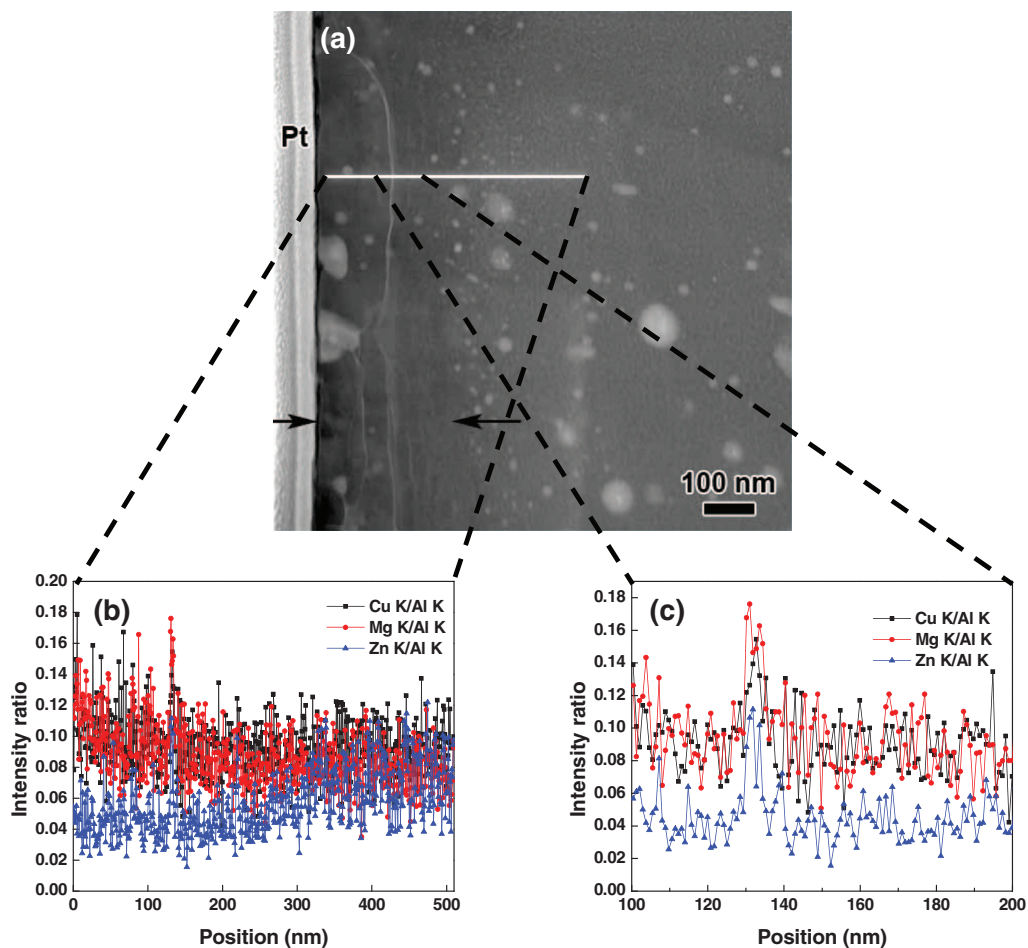
Figure 12. HAADF image and EDS line profiles of the cross-sectional AA7055-T6 sample. (a) HAADF image, (b) long EDS line profiles, and (c) short EDS line profiles across the bright band. The arrows in (a) point out the surface layer.
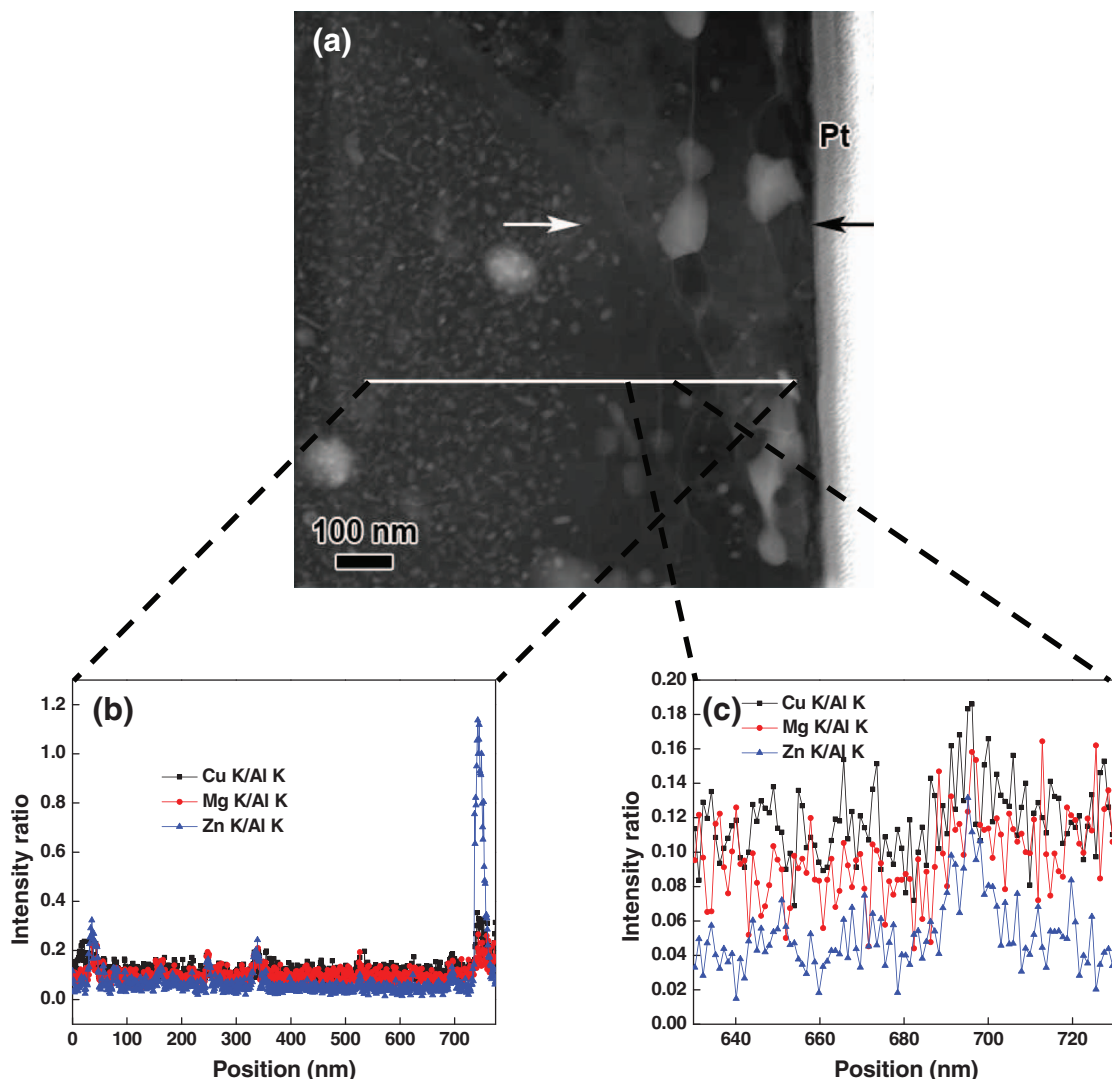
Figure 14. HAADF image and EDS line profiles of the cross-sectional AA7055-T73 sample abraded to 1200 grit. (a) HAADF image, (b) long EDS line profiles, and (c) short EDS line profiles across the bright band. The arrows in (a) point out the surface layer.

above that only one breakdown potential and no surface layer attack were observed for this temper. Dislocations are observed between the surface layer and the bulk substrate (Figure 13). However, unlike the T6 peak-aged sample, which contains fewer and smaller precipitates in the whole surface layer, there are still some precipitates in the surface layer of the T73 over-aged sample (Figure 13). The composition of the large particles in the surface layer identified by STEM/Nano-EDS is Al containing 45 wt% Cu with little of alloying elements Zn and Mg. The EDS line profiles are also shown in Figure 14. High Zn K/Al K, Mg K/Al K and Cu K/Al K at the right end of the line scan (Figure 14b) correspond to the composition of the platelet-shaped phase (Figure 14a). This suggests that the phase is likely η phase, which has a generic composition of $Mg(Zn,Cu,Al)_2$.[3,4] The composition profiles across the bright band show that the alloying elements Zn, Mg and Cu are enriched at the nano-grain boundaries (Figure 14c).

Figure 15 shows the TEM image of the cross-sectional sample from the Cu-free Al-Zn-Mg alloy in the peak-aged temper abraded to 1200 grit. This alloy, which exhibited no surface layer attack as shown above, also shows a surface layer different than the bulk substrate alloy. Similar to the AA7055-T6 alloy, the surface layer of Cu-free Al-Zn-Mg alloy contains fewer and smaller precipitates within nano-grains. Dislocations are also observed between the surface layer and the bulk substrate. The bright bands at the nano-grain boundaries are also observed in the HAADF image (Figure 16). The EDS line profiles

from the surface layer to the bulk matrix show that elemental Zn and Mg are also enriched at the nano-grain boundaries (Figure 17b).

Discussion

The localized breakdown of the AA7055-T6 alloy.— In situ observation system and cross-sectional HAADF-STEM imaging have provided considerable insight into the role of the surface layer and the localized breakdown behavior. Three potentials at which the current increased were observed for as-abraded AA7055-T6 samples. Each of the current peaks and breakdown potentials can be explained by analysis of the video images. The first breakdown potential corresponded to the transient dissolution of an active surface layer, as shown in the video of this sample.[19] TEM and HAADF results show the presence of a unique surface layer, which was different than the bulk substrate and consisted of high aspect ratio nano-grains elongated along the final abrasion direction. The alloying elements Zn, Mg and Cu were enriched at the nano-grain boundaries. Interestingly, it was observed that the surface layer dissolved faster along the final abrasion direction than any other direction. Therefore, it is likely that the layer attack propagated at the nano-grain boundaries followed by nano-grain dissolution. The exact mechanism by which the nano-grains and solute-rich bands form during polishing and grinding is still unclear. It was hypothesized that the fine precipitates are destroyed
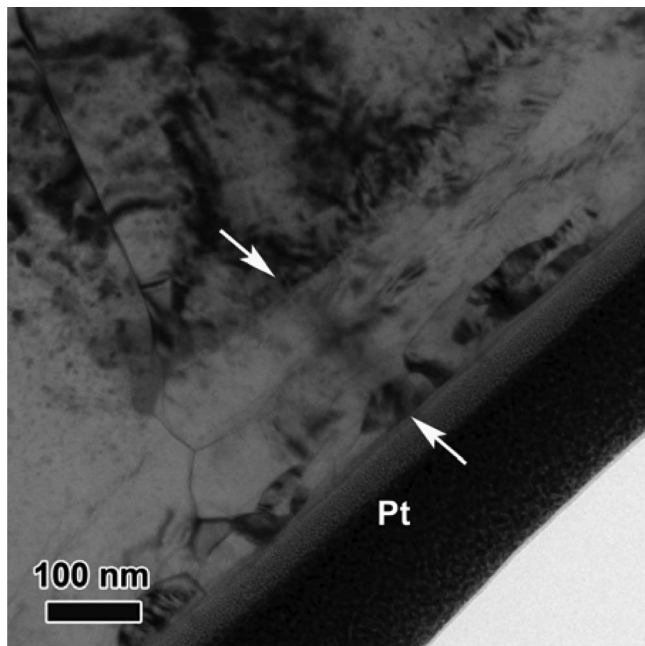
Figure 15. TEM image of the cross-sectional sample from Cu-free Al-Zn-Mg alloy in the T6 peak-aged temper abraded to 1200 grit. The arrows point out the surface layer.

or eliminated by the high shear associated with polishing and that the solute enriches in bands that are nano-grain boundaries.[11] The temperature increases arising from a periodic contact of the abrasive with the crystal surface.[25] It is likely that both shear stresses and temperature increases can lead to the formation of this disordered layer. This will be discussed in more detail in the future.

Hydrogen bubbles accumulated at the edge of the mask as the exposed surface layer was consumed, while the applied potential was increased through the second current peak. Crevice corrosion
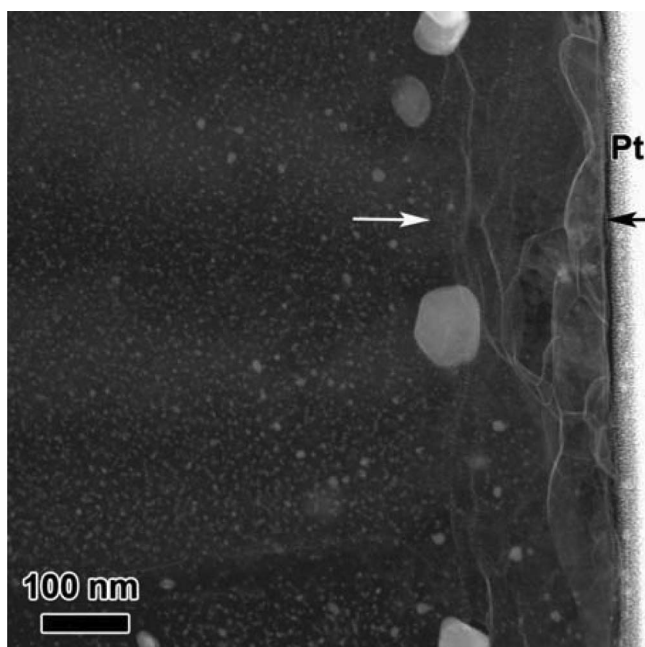
Figure 16. HAADF image of the cross-sectional sample from Cu-free Al-Zn-Mg alloy in the T6 peak-aged temper abraded to 1200 grit. The arrows point out the surface layer.
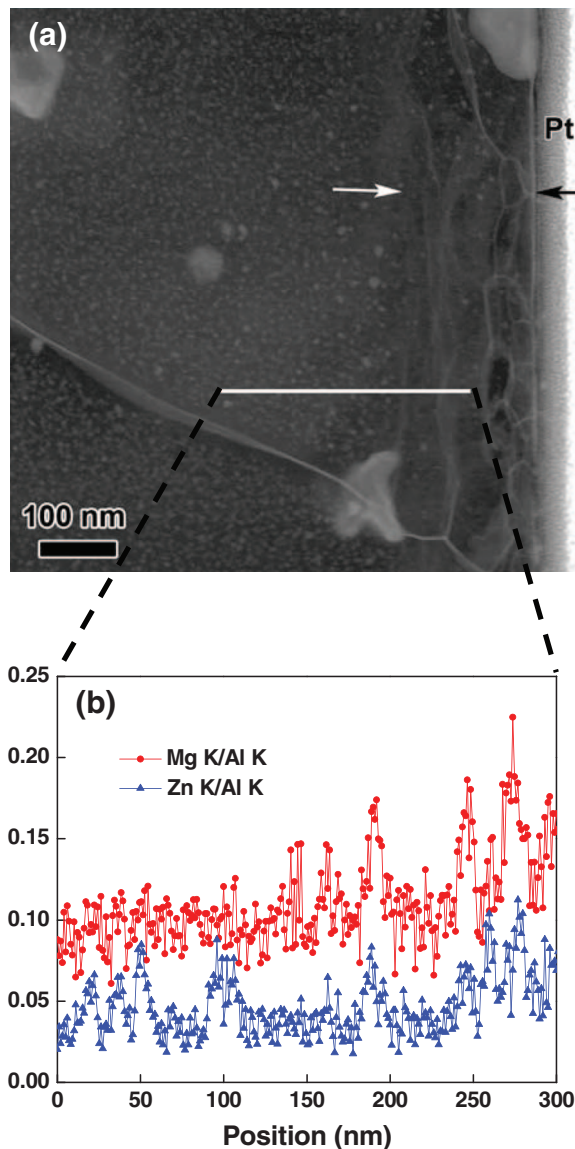
Figure 17. (a) HAADF image and (b) EDS line profiles of the cross-sectional sample from Cu-free Al-Zn-Mg alloy in the T6 peak-aged temper abraded to 1200 grit. The arrows in (a) point out the surface layer.

only occurred in samples exhibiting thin-film dissolution such as the AA7055-T6 alloy rather than the T73 over-aged alloy. As mentioned, the surface layer extended on the surface below the lacquer mask edge, which rendered this structure susceptible to crevice corrosion. Etched samples did not exhibit crevice corrosion or this current peak, since etching removed the surface layer. The crevice-free peak-aged sample showed a cathodic loop in the region of this current peak, which supports the interpretation of this peak being caused by crevice corrosion. It might be expected that the current associated with crevice corrosion under the mask would continue to increase as the ring of attack under the mask edge expands with time. However, the increasing ohmic resistance and diffusion length would tend to decrease the current density, and this can explain why a peak was observed rather than continuously increasing current. Even ignoring that, the increasing area alone cannot explain the increase in current from the background of a factor of 10 shown for this peak in Figures 1 and 2. The net anodic charge associated with crevice corrosion calculated by integrating the current over the second peak in Figure 2 is 161 mC for the ring of attack with a 5.25 mm radius. The area of the ring of attack is assumed to be 5.19 mm^2 based on measurements of the area between

the arrows and dash lines in Figure 8a. The thickness of surface layer is assumed to be 300 nm on average. Assuming layer dissolution process that was 100% current efficient, simplifying the Al matrix (87.7% Al) as 100% Al and applying Faraday's law, the charge expected for dissolution of surface layer under the mask edge is calculated to be 47 mC, which is only 29% of the measured charge associated with crevice corrosion. Part of the difference in measured and calculated charge results from local cathodic reaction in the crevice. Hydrogen bubbles were observed to emanate from the crevice indicating that some of the anodic current was consumed locally, so the assumption of the dissolution being 100% current efficient is inaccurate. However, the local cathodic reaction associated with hydrogen evolution in Al localized corrosion sites is only about 20% of the anodic reaction.[26] Therefore, if crevice corrosion alone is causing the current peak, part of the current must originate from dissolution of substrate material under the active layer at the surface under the mask edge. The large pits observed to form under the mask edge, Figure 8a, are probably the source of this current. When the surface layer under the mask edge dissolved, an aggressive crevice environment formed between the substrate material and mask edge as the result of migration of chloride into the crevice, and hydrolysis reaction of Al^{3+}, which lowers the crevice pH. As mentioned above, the rate of attack in the crevice decreased, even as the potential was increased, probably as the result of increasing ohmic and diffusional resistance, which might have been aided by the formation of corrosion products in the crevice. Crevice corrosion was observed to reinitiate as the potential was increased to higher values, which might be caused by detachment of corrosion products or just by the increased driving force of the high potential.

The second breakdown potential for the as-abraded AA7055-T6 samples was associated with pitting of the underlying bulk alloy. Elemental Cu was enriched on the exposed surface after layer dissolution[9] because the potential is far below the reversible potential for Cu dissolution. However, the Cu-enriched layer from dealloying of the surface film should not be dense and protective, which would not increase the pitting potential. Therefore, the matrix alloying content of the substrate material is responsible for the pitting potential.

After removal of the active surface layer on the as-abraded peak-aged samples by chemical etching, a single breakdown potential and no layer attack were observed in the video of this etched sample.[21] Furthermore, this single breakdown potential of the etched sample was close to the pitting potential of the as-abraded sample. Similar results were found for ion-milled samples.[11] However, the etched sample polarized in deaerated solution did not exhibit a passive region, which was found for the as-abraded samples, and it also showed residual oxygen reduction, Figures 3 and 4. As described above, the passive current density for the as-abraded samples is seen to be about 1 μA/cm², however, the passive current density was reduced after etching to a value less than the rate of residual oxygen reduction, about 0.2 μA/cm², so that the intersection of the partial anodic and cathodic curves for the etched sample polarized in deaerated solution was at the breakdown potential. Previous work has shown that etching in alkaline solution led to the removal of intermetallic particles from the alloy surface, and the development of a thin Cu-enriched layer immediately beneath a residual alumina film.[27] It has been suggested that the removal of intermetallic particles from an alkaline etched surface was responsible for the reduced current density during constant voltage anodizing in the sulfuric acid and tartaric acid.[27] Accordingly, the decrease in passive current density after etching might be attributed to the removal of intermetallic particles. The Cu-enriched layer resulting from etching, which is similar to the Cu enrichment from dealloying of the surface layer as discussed above, should not be protective, and not increase the pitting potential. Therefore, the anodic polarization behavior of the etched sample seems to represent that of the underlying bulk material, despite changes in the newly exposed surface associated with chemical etching.

Effects of Cu content on the localized breakdown behavior.— A single breakdown potential and no surface layer attack were found for the Cu-free Al-Zn-Mg alloy in the T6 peak-aged temper. However,

this alloy still shows a unique surface layer with the solute-rich bands, similar to that of the AA7055-T6 alloy exhibiting the layer attack. This indicates that the elemental Cu in the alloy plays a critical role in layer attack, because the surface layer should be active as a result of the Zn-rich bands.

For Cu-containing AA7055-T6 alloy, the attack initiated at discrete spots at the first breakdown potential because of the susceptible surface layer. The attack penetrated downward through the surface layer, but stopped at the bulk matrix, which required a higher applied potential for sustained attack because it was more resistant than the surface layer. As mentioned, the alloying elements Zn and Mg in the precipitates were concentrated into solute-rich bands in the thin surface layer during grinding, which made this layer susceptible to attack. On the other hand, Cu in the solid solution of the bulk substrate ennobled the pitting corrosion.[28] Both reasons contributed to the activity gap between the surface layer and bulk substrate. Therefore, the attack propagated outward and growed fast along the nano-grain boundaries in the surface layer, instead of penetrating into the bulk alloy. It is remarkable that the attack did not propagate into the underlying bulk alloy because the interface was not protected by the presence of a passive film. When the attack penetrated through the surface layer, the metal matrix was exposed to the local environment, which was acidic and contained high chloride content for the reasons described above. The fact that the pitting potential for the etched samples, which are covered with a passive film, is similar to the second breakdown potential for the as-abraded samples indicates that the repassivation potential for this material is close to the pitting potential.

For the Cu-free Al alloy in the peak-aged condition, however, the absence of surface layer attack indicates that there is no obvious difference in breakdown potential between the surface layer and the underlying bulk. The thin surface layer containing nano-grains with the solute-rich bands was observed in this Cu-free alloy, which, according to the reasoning just described, suggests that the layer should be susceptible to enhanced attack. However, the matrix solid solution of the bulk substrate contains only alloying elements Zn and Mg. Muller and Galvele showed that Zn decreased the pitting potential of aluminum, while Mg had almost no effect on the pitting potential.[29] Therefore, the activity gap between the surface layer and bulk alloy is not evident, so the attack initiated at specific spots and propagated through the surface layer into the underlying bulk matrix without thin-film dissolution. Because of the absence of Cu in solid solution, the pitting potential of the Cu-free alloy in the peak-aged condition is much lower than that of the AA7055-T6 alloy.

No surface layer attack and only one breakdown potential were observed for AA7055-T73 over-aged samples with different roughness, which behaved similar to the Cu-free alloy in the peak-aged condition. It should be noted that, unlike the AA7055-T6 alloy, some precipitates exist in the surface layer of the T73 over-aged alloy. It is possible that η precipitates, which are large and incoherent with the Al matrix, are bypassed by moving dislocations. However, η′ phases in the AA7055-T6 alloy are smaller and coherent with the Al matrix, which are cut by dislocation.[30] Nevertheless, the Zn, Mg and Cu rich bands in the surface layer were also observed for the T73 over-aged alloy, which should render the layer susceptible. Surface layer dissolution depends on the relative susceptibility of the surface layer and underlying matrix. To identify the polarization behavior for the T73 over-aged alloy, it is necessary to understand details of the microstructure. The compositions of precipitates and matrix solid solution of three 7××× series Al alloys were studied by combining APT and ASAXS techniques.[7] The Cu content in the precipitates was close to the alloy content at low aging temperature (120°C), while the Cu content in the precipitates increased with increasing temperature and Cu alloy content, which was attributed to the slower diffusivity of Cu element. This result is in agreement with the work of Ramgopal and Frankel,[4] which showed that the Cu concentration in the grain-boundary precipitates for the AA7150-T7 alloy (aged at 120°C for 24 h followed by 160°C for 21 h) was much higher than for the T6 peak-aged alloy (aged at 120°C for 24 h). As a result, the total matrix solute content was much lower for the over-aged alloy as compared to the peak-aged alloy. Furthermore,

the Cu content of the precipitates composition for the over-aged alloy was higher than that for the peak-aged alloy, which in turn reveals that the Cu content in the matrix solid solution for the over-aged alloy was lower compared to the peak-aged alloy. This understanding can be used to explain the polarization behavior of the over-aged alloy. Like the Cu-free alloy, the pitting potential of the bulk over-aged alloy is not ennobled due to low Cu content in solid solution. So even though the surface layer with the Zn-rich bands should be susceptible, layer attack was not observed because the difference in breakdown potential between the layer and bulk alloy is small.

As described above, the preferential dissolution of the surface layer is due to a difference in breakdown potential between the surface layer and the underlying bulk. Both the Zn-rich bands in the surface layer and the Cu content in matrix solid solution of the underlying bulk alloy contribute to the activity gap between them.

Effects of temper on the localized breakdown behavior.— Two typical tempers in AA7055 alloy were chosen to investigate the effects of aging treatments on the polarization behavior. It is necessary to understand the effects of aging treatment on the matrix and precipitate compositions. The matrix composition evolution of 7050 Al alloy aged up to 24 h at 121°C was investigated using APT.[2] The concentrations of Zn and Mg in the matrix solid solution decreased with aging time as a result of precipitation during aging. The Cu concentration in solid solution showed a constant but slow decrease with aging. As mentioned above, however, the Cu content in the precipitates increased with increasing temperature due to the slower diffusivity of elemental Cu. The Zn, Mg and Cu contents in the matrix solid solution for the over-aged alloy were lower than those for the peak-aged alloy.

The understanding of the precipitates and matrix solute compositions allows new insight into the effects of temper on the polarization behavior. The pitting potential of the AA7055-T6 alloy (about −700 mV SCE) was more noble than that of the T3 over-aged alloy (about −770 mV SCE). As discussed above, both the Cu and Zn matrix concentrations were lower for the T73 over-aged alloy due to more precipitation and more Cu incorporation in the precipitates. Alloying elements Cu and Zn have opposite effects on the pitting potential of Al alloys. The decrease in pitting potential from peak-aged to over-aged tempers indicates that the effects of changes in the matrix Cu content dominate the effects of changes in the matrix Zn content. However, the pitting potential increased with aging time during the under-aged and peak-aged states,[11–13] which was considered to result from depletion of Zn content in solid solution causing an increase in matrix breakdown potential. The Zn to Cu ratio in the matrix compositions controls the pitting potential of the Cu-containing AA7××× series alloys with different tempers. For under-aged alloys, the matrix Zn content controls the pitting potential because of high Zn solute content, while the effect of Cu in solid solution is not obvious. During over-aging from the T6 peak-aged to T7 over-aged tempers, a decrease in Cu content leads to a decrease in pitting potential, even though the Zn solute content continues to decrease. This is due to a low Zn concentration during the over-aged states.

Conclusions

The corrosion behavior and microstructure were studied for AA7055 alloy and a Cu-free Al-4.59Zn-1.48Mg alloy with different tempers and surface preparation using an in situ observation system and STEM. The following can be concluded:

1. Like other 7xxx series Al alloys, an altered surface layer with microstructure containing solute-rich bands can form on AA7055 alloy and a Cu-free Al-4.59Zn-1.48Mg alloy during surface preparation by abrading with grinding paper.
2. Surface layer attack at low potentials can happen on 7xxx series Al alloys when there is a difference in breakdown potential between the surface layer and the underlying bulk alloy. Both the Zn-rich bands that form in the surface layer as a result of abrasion with grinding paper and the Cu content in the solid solution of the underlying bulk alloy contribute to the gap in susceptibility.
3. The pitting potential decreased from peak-aged to over-aged tempers. The change in pitting potential with over-aged tempers can be rationalized based on the Cu content in the matrix solid solution.

References

1. A. Deschamps, F. Livet, and Y. Brechet, *Acta Mater.*, **47**, 281 (1999).
2. G. Sha and A. Cerezo, *Acta Mater.*, **52**, 4503 (2004).
3. J. E. Hatch, Editor, *Aluminum: Properties and Physical Metallurgy*, ASM, Metals Park, OH (1984).
4. T. Ramgopal, P. I. Gouma, and G. S. Frankel, *Corrosion*, **58**, 687 (2002).
5. A. Deschamps, A. Bigot, F. Livet, P. Auger, Y. Brechet, and D. Blavette, *Philos. Mag. A*, **81**, 2391 (2001).
6. M. Dumont, W. Lefebvre, B. Doisneau-Cottignies, and A. Deschamps, *Acta Mater.*, **53**, 2881 (2005).
7. T. Marlaud, A. Deschamps, F. Bley, W. Lefebvre, and B. Baroux, *Acta Mater.*, **58**, 248 (2010).
8. S. Maitra and G. C. English, *Metall. Mater. Trans. A*, **12**, 535 (1981).
9. Q. Meng and G. S. Frankel, *J. Electrochem. Soc.*, **151**, B271 (2004).
10. R. S. Huang, C. J. Lin, and H. S. Isaacs, *Electrochem. Solid-State Lett.*, **9**, B11 (2006).
11. Z. Zhao and G. S. Frankel, *Corros. Sci.*, **49**, 3064 (2007).
12. Z. Zhao and G. S. Frankel, *Corros. Sci.*, **49**, 3089 (2007).
13. M. Kappes, L. Kovarik, M. J. Mills, G. S. Frankel, and M. K. Miller, *J. Electrochem. Soc.*, **155**, C437 (2008).
14. D. H. Shin, I. Kim, J. Kim, and K. T. Park, *Acta Mater.*, **49**, 1285 (2001).
15. T. Hebesberger, H. P. Stüwe, A. Vorhauer, F. Wetscher, and R. Pippan, *Acta Mater.*, **53**, 393 (2005).
16. P. J. E. Forsyth, *Mater. Sci. Technol.*, **14**, 151 (1998).
17. A. Afseth, J. H. Nordlien, G. M. Scamans, and K. Nisancioglu, *Corros. Sci.*, **43**, 2093 (2001).
18. X. Wu, N. Tao, Y. Hong, B. Xu, J. Lu, and K. Lu, *Acta Mater.*, **50**, 2075 (2002).
19. Supplemental material, Video 1.
20. J. R. Galvele, *J. Electrochem. Soc.*, **123**, 464 (1976).
21. Supplemental material, Video 2.
22. Supplemental material, Video 3.
23. J. Chen, L. Zhen, S. Yang, W. Shao, and S. Dai, *Mater. Sci. Eng. A*, **500**, 34 (2009).
24. L. Kovarik and M. J. Mills, *Scripta Mater.*, **64**, 999 (2011).
25. A. D. Vlasov, J. S. Rez, and M. L. Filchenkov, *Cryst. Res. Technol.*, **23**, 1093 (1988).
26. G. S. Frankel, *Corros. Sci.*, **30**, 1203 (1990).
27. Y. Ma, X. Zhou, G. E. Thompson, X. Zhang, C. Luo, M. Curioni, and H. Liu, *J. Electrochem. Soc.*, **160**, C111 (2013)
28. I. L. Muller and J. R. Galvele, *Corros. Sci.*, **17**, 179 (1977).
29. I. L. Muller and J. R. Galvele, *Corros. Sci.*, **17**, 995 (1977).
30. P. Guyot and L. Cottignies, *Acta Mater.*, **44**, 4161 (1996).